Experimental and Theoretical Determination of the Effective Penetration Depth of Ultrafast Laser Radiation in Stainless Steel

Daniel Metzner[1] ⬤ · Markus Olbrich[1] · Peter Lickschat[1] · Alexander Horn[1] ·
Steffen Weißmantel[1]

Abstract

This study intends to present a simple two-temperature model (TTM) for the fast calculation of the ablation depth as well as the corresponding effective penetration depth for stainless steel by considering temperature-dependent material parameters. The model is validated by a comparison of the calculated to the experimentally determined ablation depth and the corresponding effective penetration depth in dependence on the pulse duration (200 fs up to 10 ps) and the fluence. The TTM enables to consider the interaction of pulsed laser radiation with the electron system and the subsequent interaction of the electrons with the phonon system. The theoretical results fit very well to the experimental results and enable the understanding of the dependence of the ablation depth and of the effective penetration depth on the pulse duration. Laser radiation with a pulse duration in the femtosecond regime results in larger ablation depths compared to longer-pulsed laser radiation in the picosecond regime. Analogously to the ablation depth, larger effective penetration depths are observed due to considerably higher electron temperatures for laser radiation with pulse durations in the femtosecond regime.

Keywords Penetration depth · Ultrashort-pulsed laser radiation · Ablation ·
Two-temperature model

Introduction

Ultrafast laser radiation enables highly efficient material processing, especially in laser micromachining with minimal thermal stress [1]. As a result, a large number

---

✉ Daniel Metzner
 metzner@hs-mittweida.de

[1] University of Applied Sciences, Technikumplatz 17, 09648 Mittweida, Germany

of materials can be processed with minimal lateral damage and a very small heat-affected zone [2, 3]. Due to the extremely short pulse duration, the pulse energy is deposited into the electron system within the pulse duration time of a few hundreds of femtoseconds, and is transferred to the phonon system within the electron-phonon relaxation time, being in the range of a few picoseconds. If the amount of absorbed energy exceeds a material-dependent threshold, the material is ablated. Additionally, during the interaction between the laser radiation and the material, a diffusion of energy within the electron system occurs, which increases the energy density below the surface, and thus, may cause ablation up to an effective penetration depth. The effective penetration depth depends on the pulse duration and the fluence of the laser radiation. Therefore, by knowing the resulting penetration depth as a function of the pulse duration and fluence, the ablation depth, and thus, the ablation rate can be controlled. The ablation rate is important for industrial applications, such as laser micro-structuring, laser engraving or laser cutting, particularly for stainless steel.

The ultrafast excitation of metals is often described by the two-temperature model [4]. It is assumed that the excitation of the electrons by the laser radiation is followed by a rapid local thermalization of the electrons, and followed by the subsequent thermalization between the electrons and the phonons. This thermal process is described by two different temperature distributions, one for the electron system and one for the phonon system. The two temperature distributions depend on space and time, and their evolution is defined by two coupled differential equations describing the energy transfer between the two systems and the heat diffusion within each system. Due to the energy transfer, the phonon system may be heated up sufficiently so that ablation can occur. Due to the lack of knowledge of the temperature-dependent parameters, such as the reflectivity of the laser radiation, the absorption coefficient, or the electron-phonon coupling factor, the temperature dependency of the parameters was approximated by simple relations and assumed to be temperature-independent like in previous simulations of the interaction of ultrashort pulses with steel (or iron) which were already performed using the two temperature model [5–7]. Another possibility to calculate the ablation rate of steel or iron using ultrashort pulses is the molecular dynamic simulation technique [8, 9]. However, this simulation method requires a very high computing effort and also the knowledge of functional relationships between material-specific parameters and the electron temperature.

Experimental ablation studies on steel have demonstrated, that the effective penetration depth of ultrafast laser radiation can be much larger than the optical penetration depth [10–14]. In the current state of the art, the effective penetration depth is derived from the ablation depth or the ablated volume of a cavity produced by a single pulse or multiple pulses [10–14]. Nevertheless, large errors are obtained by measuring the ablation depth or the ablated volume induced by a single pulse. Another possibility to determine the effective penetration depth with a simultaneous reduction of the errors is given by the measurement of the ablation depth or the ablated volume of a cavity produced by multiple pulses. On the other hand, for multiple irradiations, the measurement of the required depths or volumes are more accurate, but the effective penetration depth differs from the values obtained from single-pulse experiments due to the incubation effect [15–17] induced by multiple irradiations.

To verify the experimental data and to obtain more accurate predictions, the ablation depth is simulated in this work by a relatively simple numerical approach of the two coupled equations of the two-temperature model, and an associated effective penetration depth is calculated. In contrast to the present state of the art, the temperature dependence of material-specific parameters such as the reflectance of the laser radiation, the thermal conductivity and the volumetric heat capacity is taken into account. This simulation model is intended to improve the precision of the ablation process for industrial applications of laser micro-structuring in a simple and fast way.

Theoretical Background

Two-Temperature Model

To calculate the heat propagation in the material, the two-temperature model is used [4, 18–21], in which the evolution of the electron temperature T_e is described by

$$C_e \partial_t T_e = \nabla \cdot (\lambda_e(T_e) \nabla T_e) - G(T_e - T_{ph}) + S, \tag{1}$$

and the phonon temperature T_{ph} is given by

$$C_{ph} \partial_t T_{ph} = \nabla \cdot (\lambda_{ph} \nabla T_{ph}) + G(T_e - T_{ph}). \tag{2}$$

In the two equations, connected through the coupling term G, $C_e(T_e)$ and C_{ph} represent the volumetric heat capacities and the parameters $\lambda_e(T_e)$ and λ_{ph} define the thermal conductivity of the electron and phonon system. The heat source (laser radiation) is characterized by the variable S. The phase state is considered with the volumetric heat capacity of the phonons

$$C_{ph} = \rho \left[c_{p0} + \frac{\Delta H_M}{\Delta T \sqrt{2\pi}} \exp\left(-0.5 \left(\frac{T_{ph} - T_M}{\Delta T}\right)^2\right) \right] \tag{3}$$

with the latent heat of fusion [22] ΔH_M. The volumetric heat capacity of the electron system

$$C_e(T_e) = \left[2.677 \times 10^6 \exp\left(8.937 \times 10^{-6} T_e/K\right) \right.$$
$$\left. -2.987 \times 10^6 \exp\left(-0.0003787 T_e/K\right) \right] \mathrm{JK^{-1}m^{-3}} \tag{4}$$

and the coupling factor

$$G = \left[2.837 \times 10^{18} \exp\left(-\left(\frac{T_e/K - 3077}{1.166 \times 10^4}\right)^2\right) \right.$$
$$\left. +2.993 \times 10^{18} \exp\left(-\left(\frac{T_e/K - 2.988 \times 10^4}{8.147 \times 10^4}\right)^2\right) \right] \mathrm{WK^{-1}m^{-3}}$$
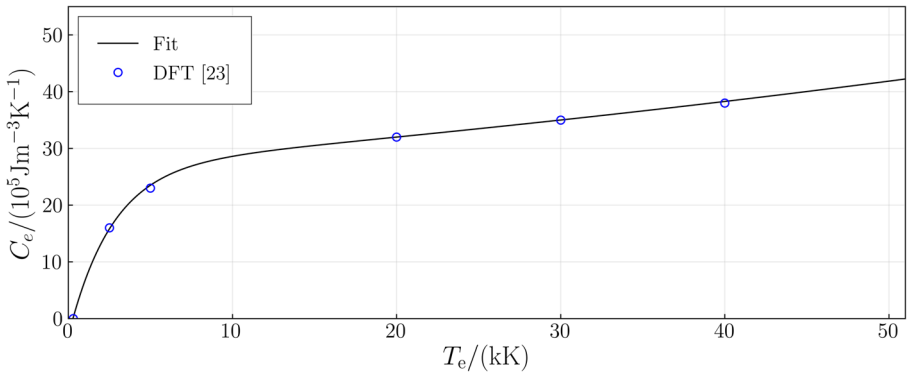
Fig. 1 Volumetric heat capacity of the electrons C_e as a function of the electron temperature T_e for stainless steel. The solid line represents the fitted function and the open circles the values of the DFT-calculations [23]

are fitted according to the theoretical results of the density-functional-theory (DFT)-calculations [23] (Figs. 1 and 2). The dependence of the thermal conductivity [23] of the electrons λ_e on the electron temperature is given by

$$\lambda_e(T_e) = \left[\left(0.535 \times 10^{-4} \, T_e/\text{K} - 0.004 \right) \times 10^3 \right] \text{WK}^{-1}\text{m}^{-1} \qquad (5)$$

and is visualized in Fig. 3. The thermal conductivity of the phonon system [24] ($\lambda_{ph} = 23 \, \text{W m}^{-1}\text{K}^{-1}$) is neglected as the condition $\lambda_e \gg \lambda_{ph}$ is fulfilled for $T_e > T_0$.

The heat source S can be described as

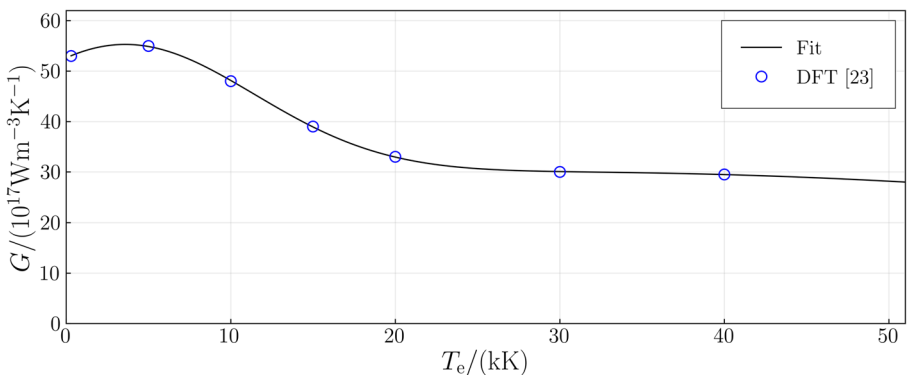$$S = (1 - R(T_e))\alpha(z) \, I(t) \, I(x, y, z) \qquad (6)$$

Fig. 2 Coupling factor G as a function of the electron temperature T_e for stainless steel. The solid line represents the fitted function and the open circles the values of the DFT-calculations [23]
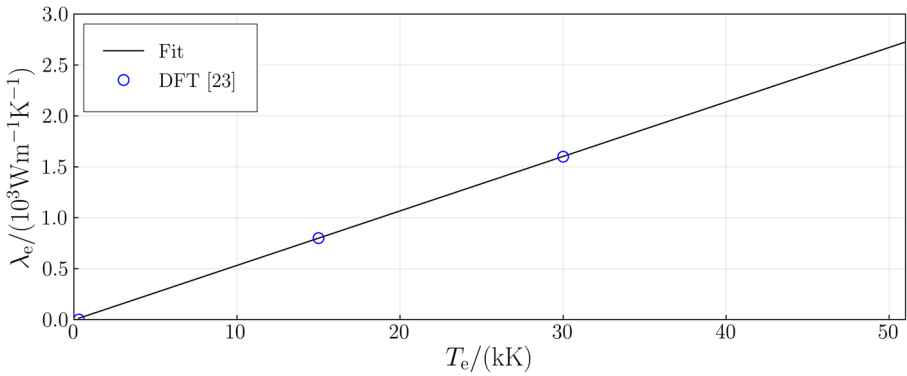
Fig. 3 Numerically determined thermal conductivity λ_e as a function of the electron temperature T_e for stainless steel [23]. The solid line represents the fitted function

with a gaussian-shaped temporal intensity distribution

$$I(t) = I_0 \exp\left[-4\ln2\frac{(t - t_0)^2}{\tau_H^2}\right] \tag{7}$$

with the laser peak intensity

$$I_0 = \sqrt{\frac{4\ln2}{\pi}} \frac{H_0}{\tau_H}, \tag{8}$$

where H_0 represents the laser peak fluence and τ_H the pulse duration. The peak intensity I_0 is given at $t_0 = 2\,\tau_H$. In order to simplify the simulations, the spatial intensity distribution in the surface plane $I_{x,y}$ is not taken into account and only one-dimensional simulations with the peak intensity I_0 at $x = y = 0$ are considered. The spatial intensity distribution in the depth z is derived by Beer's law

$$I(z) = I_0 \exp\left(-\int_{z_0}^{z} \alpha(z)\,\mathrm{d}z\right), \tag{9}$$

where I represents the laser intensity, z the material depth, z_0 the position of the surface and $\alpha = \frac{4\pi\,\kappa(T_e)}{\lambda}$ the linear absorption coefficient. By integrating Eq. 9 under the assumption of an effective value $\alpha = \frac{1}{\delta_{opt}}$, the so called reciprocal optical penetration depth averaged over space and time an approximation of the fluence H follows

$$H(z) = H_0 \exp\left(-\alpha\,z\right). \tag{10}$$

In [25] the calculated temperature dependent optical properties for Fe, Cr and Ni were presented. By weighting the major elements of 316L (Fe70Cr17Ni13) the reflectance R and the extinction index κ as a function of the electron temperature is

$$R(T_e) = \left[11 \exp(-0.00013\,T_e/\mathrm{K}) + 59.2\right]\,\%. \tag{11}$$

and

$$\kappa(T_e) = 1.4 \exp(-0.00015\,T_e/\mathrm{K}) + 3.75 \tag{12}$$

(Figs. 4 and 5). The results of the DFT simulations presented in [23] and in [25] were performed up to an electron temperature of 25×10^3 K. Based on Eqs. 4, 5,
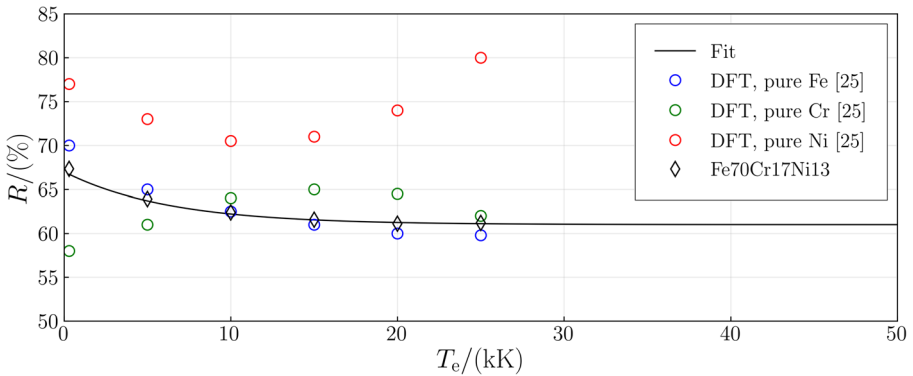
Fig. 4 Reflectance R as a function of the electron temperature T_e for pure iron, chromium, nickel and a weighting of the major elements of 316L (Fe70Cr17Ni13) at a wavelength $\lambda = 1030\,\text{nm}$ [25]. The solid line represents the fitted function Eq. 11

11 and 12,the material-specific and optical properties at higher electron temperatures are extrapolated in this study. The other required material-specific parameters for solving Eqs. 1 and 2 for stainless steel are given in Table 1. For the case that no data are available for stainless steel, the data for iron is used instead.

By irradiating a material using ultrafast laser radiation the temperature of the phonon system increases within the heating time τ_{heat}, being defined by $\tau_{\text{heat}} = \max\{\tau_{\text{e-ph}}; \tau_{\text{H}}\}$, wherein $\tau_{\text{e-ph}} = \left(\frac{1}{C_e} + \frac{1}{C_{\text{ph}}} \right)^{-1} G^{-1}$ [26, 27] represents the electron-phonon relaxation time or also called electron-phonon coupling time in the absence of ablation, and τ_{H} the pulse duration. By increasing the temperature of the phonon system, thermal stress is induced, which usually induces a thermal expansion of the material in the case of slow heating, and therefore unloading and reduction of the induced thermal stress. The time scale needed for the reduction of the thermal stress
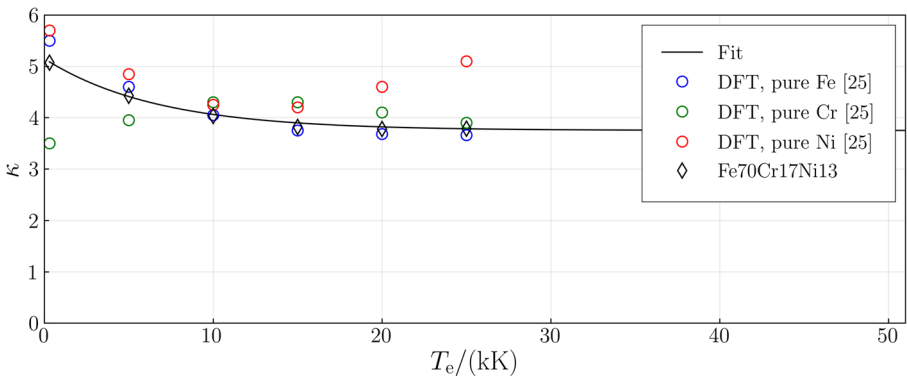

Fig. 5 Extinction coefficient κ as a function of the electron temperature T_e for pure iron, chromium, nickel and a weighting of the major elements of 316L (Fe70Cr17Ni13) at a wavelength $\lambda = 1030\,\text{nm}$ [25]. The solid line represents the fitted function Eq. 12

Table 1 Material-specific parameters for steel and iron

Parameter	Value
Density [48] ρ	7.95 g/cm^3 @ 300 K
Specific heat capacity [48] c_{p0}	450 J/(kgK) @ 300 K
Melting temperature [49] T_M	1811 K
Critical temperature [50] T_c	9250 K (iron)
Heat of fusion [51] ΔH_M	13.8 KJ/mol (iron)
ΔT used for Eq. 3	50 K
Threshold fluence [52] $H_{th,low}$	0.23 J/cm^2
Threshold fluence [13] $H_{th,high}$	1.2 J/cm^2

is called acoustic relaxation time $\tau_{ac} = L_{th}/c_s$ [28] and is determined by the thermal diffusion length L_{th} and the speed of sound c_s. In the case of irradiating a metal with ultrafast laser radiation, the condition $\tau_{heat} < \tau_{ac}$ is fulfilled, being called stress confinement [28, 29]. Within τ_{heat} the thermal expansion is neglectable and nearly isochoric heating of the material in conjunction with a large increase of the pressure as well as a phase change from solid to liquid is obtained (white to purple trajectories in Fig. 6). The induced pressure decays into two shock waves propagating in opposite directions, whereby one shock wave propagates into the material, and the other shock wave propagates towards the surface. The shock wave propagating towards the surfaces is reflected at the surfaces according to the wave impedance at the interface, and the shock wave is transformed into a rarefaction wave [23, 28–30]. Consequently, a pair of shock and rarefaction waves propagate into the material. The emission of the shock waves also enables the thermal expansion of the material, and heat transfer to surrounding material occurs during this relaxation process, resulting in a decrease of the density and the temperature (Fig. 6). The tensile stress of the rarefaction wave transforms the stable liquid into a metastable liquid, in which the binodal is crossed, and cavitation below the surface is induced if the time under negative pressure exceeds the time for forming a stable bubble. As a result, the spallation
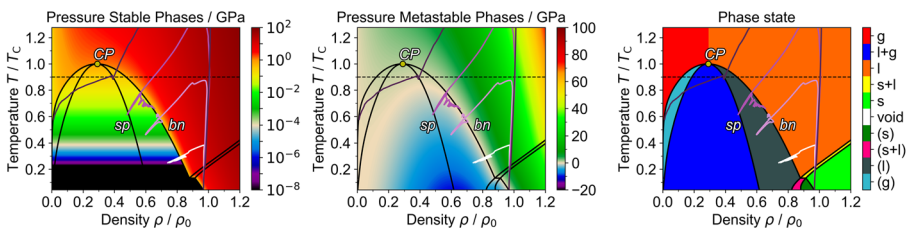

Fig. 6 Schematic temperature-density-pressure and phase diagram according to [33–39] including four typical trajectories of a point slightly below the surface for spallation: white and light purple, and for phase explosion: purple and dark purple. The darker the color of the trajectory, the higher the fluence of the laser radiation. Different colors in the phase diagram correspond to different phase states (g, l+g, l, s+l, void), wherein metastable phases are indicated by brackets ((s), (s+l), (l), (g)). The dot represents the critical point CP with the critical temperature T_c, the critical density ρ_c as well as the critical pressure p_c, bn the binodal, and sp the spinodal, respectively

of layers of liquid material occurs. For higher fluences, and thus, higher temperatures of the material, the relaxation of the material results further in the crossing of the spinodal, why a fast-expanding liquid-vapor mixture is formed. This process is called phase explosion, explosive boiling, or spinodal decomposition, whereby in most cases, phase explosion is used. In contrast to spallation, representing a thermo-mechanical process, phase explosion represents mainly a thermodynamic process if only the ablated material is considered and the induced shock wave due to the recoil pressure of the ablated material is neglected. As a general rule based on the trajectories in the phase diagram (Fig. 6), spallation occurs if the maximum temperature is smaller than 90 % of the thermodynamic critical temperature T_c [31], and phase explosion occurs if the maximum temperature is larger than $T_{c,0.9}$. The result of $T_{c,0.9}$ based on the mentioned hydrodynamic descriptions is consistent with pure thermodynamic descriptions [32].

The phase explosion and the material removal of metals have been studied extensively [13, 17, 21, 40, 41]. However, most studies examined the thermal ablation within a low-fluence regime or within a high-fluence regime, in which the two regimes differ primarily in the ablation rate. The threshold fluence for stainless steel of the low fluence regime $H_{thr,low}$ and the threshold fluence of the high fluence regime $H_{thr,high}$ are presented in Table 1.

As the intention of the article is given by presenting a simple model, all hydrodynamic processes in conjunction with an equation of state [33–35] are neglected, and only the evolution of the electron and the phonon temperature is considered. The ablation criterion is defined to be $T_{c,0.9}$ [42–44], representing phase explosion. Therefore, spallation, occurring for fluences slightly above the ablation threshold of the low fluence regime, and representing the dominant ablation mechanism for temperatures up to $T_{c,0.9}$, is not taken into account. Thus, the applied model is only applicable for fluences well above the ablation threshold of the low fluence regime.

Due to the fast isochoric laser-induced heating up to $T_{c,0.9}$, no phase change from liquid to vapor, and thus, no evaporation occurs (Fig. 6). Therefore, the enthalpy of evaporation is neglected in the simulations. This assumption is supported by the fact, that the enthalpy of evaporation decreases for temperatures larger than the boiling temperature at normal conditions [45], and no enthalpy of evaporation exists for $T > T_c$. Concluding, and also defined in Eq. 3, only the enthalpy of fusion has to be considered. Furthermore, the density of the material is assumed constant in the simulations.

In the case of ablation of material, the ablated particles feature an average velocity of about 100 m/s [46]. Furthermore, the material surface is heated up to $T_{c,0.9}$ within a few picoseconds due to the fast energy transfer from the electron to the phonon system, and thus, ablation starts already within this time. Nevertheless, the ablated particles propagate only a few angstroms away from the surface during this time of a few picoseconds. Thus, an interaction of the free electrons from the ablation cloud with the non-ablated material is still probable. Therefore, in the simulations, only the temperature of the phonon system is limited to a maximum of $T_{c,0.9}$ and the ablation of material is only related to the phonon system. The electron system can reach much higher temperatures and is excluded from the ablation. The electrons can therefore heat the phonons up to the thermodynamic equilibrium between the two systems

even if ablation has already occurred. The time to reach thermodynamic equilibrium is defined in this work as the electron-phonon coupling time $\tau_{\text{e-ph}}$. The material thickness is regarded as infinite, so that a geometrically induced heat accumulation is prevented. The initial temperatures are set to be 300 K. The Eqs. 1 and 2 are solved numerically by applying the finite differences method for the spatial derivatives and the Euler method for the time integration.

For a quantitative statement about the ablation process, a 1D simulation during the interaction is sufficient as thermal diffusion can be neglected during the time scale of a few 10 ps due to the large aspect ratio $d_0/L_{\text{th}} \approx 169$ of the laser spot size $d_0 = 30\,\mu\text{m}$ and the thermal diffusion length $L_{\text{th}} = \sqrt{\pi\,\lambda_{\text{e}}/C_{\text{e}}\,t} \approx 177\,\text{nm}(\lambda_{\text{e}} \approx 1.5 \times 10^3\,\text{W/(m K)}, C_{\text{e}} \approx 30 \times 10^5\,J/(\text{m}^3\,K), t = 20\,ps)$ [47].

The Effective Penetration Depth

Many studies in the recent years have demonstrated a much deeper transport of the absorbed energy into the material, compared to the optical penetration depth by absorption of the laser radiation, due to the effect of ballistic motion and the diffusion of hot electrons [43, 53–56]. The increased absorption depth has to be considered by an effective absorption coefficient in the source term in Eq. 6 including the optical and ballistic penetration depth [47]. In the simulations, the ballistic penetration depth is not considered as this value is not known. Nevertheless, the experimental determination of an effective penetration depths differs from a numerical one, as the experimental penetration depth includes further the thermal diffusion length. Thus, the experimental effective absorption coefficient α_{eff} is defined by

$$\alpha_{\text{eff}}(T_{\text{e}}) = \frac{1}{\delta_{\text{opt}}(T_{\text{e}}) + \delta_{\text{ball}}(T_{\text{e}}) + \delta_{\text{diff}}(T_{\text{e}})} = \frac{1}{\delta_{\text{eff}}(T_{\text{e}})}, \tag{13}$$

including the reciprocal sum of the optical penetration depth $\delta_{\text{opt}}(T_{\text{e}})$, the depth of the ballistic electrons $\delta_{\text{ball}}(T_{\text{e}})$, and the thermal diffusion length of the hot electrons $\delta_{\text{diff}}(T_{\text{e}})$, with δ_{eff} as the effective penetration depth.

In order to calculate the effective penetration depth in accordance to the experimental methods in the low fluence regime [57–60], the threshold fluence $H_{\text{th,low}}$ is substituted in Eq. 10 and z_{abl} for z, resulting in

$$H_{\text{th,low}} = H_0 \exp\left(-\frac{1}{\delta_{\text{eff}}}\,z_{\text{abl}}\right). \tag{14}$$

Thus, by knowing the fluence H_0, the threshold fluence $H_{\text{th,low}}$, and the ablation depth z_{abl}, the effective penetration depth

$$\delta_{\text{eff}}(T_{\text{e}}) = \frac{z_{\text{abl}}}{\ln\left(\frac{H_0}{H_{\text{th,low}}}\right)} \tag{15}$$

can be determined.

For the calculation of the effective penetration depth in the high fluence regime an analytical method was presented, which was derived from the two temperature model [61]. The model assumes a constant coupling factor G, a constant reflectance R, and the constant volumetric heat capacity C_{e}. Consequently, the effective penetration

depth is independent of the electron temperature, and thus also independent of the pulse duration. Another method [10] to calculate the effective penetration depth in the high fluence regime is given by

$$\delta_{\text{eff}}(T_{\text{e}}) = \frac{z_{\text{abl}}}{\sqrt{\ln\left(\frac{H_0}{H_{\text{th,low}}}\right)}}, \tag{16}$$

which represents an approximation of the fluence-dependent ablation depth in the thermal diffusion model [62].

Experimental Details

A solid-state laser (Pharos, Light Conversion) with a variable pulse duration in the range of 200 fs up to 10 ps and an emitting wavelength of 1030 nm is used for the experiments. The spatial intensity distributions nearly equals an ideal spatial gaussian profile ($M^2 < 1.1$). A spherical lens with a focal length of 167 mm is used for focusing the laser radiation to a beam waist radius of 15 μm on the material surface.

Stainless steel (316L) with a thickness of 0.5 cm is used as the target material for the laser ablation. The ablation structures in the form of a micro blind hole are created with single-pulsed laser radiation with a fluence of 0.75 J/cm^2 in the low fluence regime, and with a fluence of 3.0 J/cm^2 as a representative for the high fluence regime, all for a pulse duration of 200 fs up to 10 ps. The ablation depth of the ablation structures are measured by confocal microscopy (Fig. 7).

Results and Discussion

Simulation Results

In order to investigate the dependence of the ablation depth on the pulse duration, the pulse duration is varied in a range between 200 fs and 10 ps. Furthermore, the ablation threshold tends to be independent on the pulse duration in this range [10]. Furthermore, all other laser parameters of the experiments were used, namely the wavelength of 1030 nm, a peak fluence of H_0 of 0.75 J/cm^2 in the low fluence regime and 3.0 J/cm^2 in the high fluence regime [5, 10, 63]. In the following, the evolution of the temperature distribution on the material surface and in the material depth z is discussed using a pulse duration of 200 fs and 10 ps exemplary. The temperature distribution as a function of time is presented in Fig. 8 for 200 fs and in Fig. 9 for 10 ps.

The comparison of the temperatures for the two pulse durations at the same fluence demonstrates that a much higher electron temperature is obtained at 200 fs. With longer pulse durations, the intensity of the pulse decreases according to Eq. 8, while the fluence remains constant. As a result, the lower electron temperature is observed for pulse durations in the picosecond regime compared to the pulse durations in the
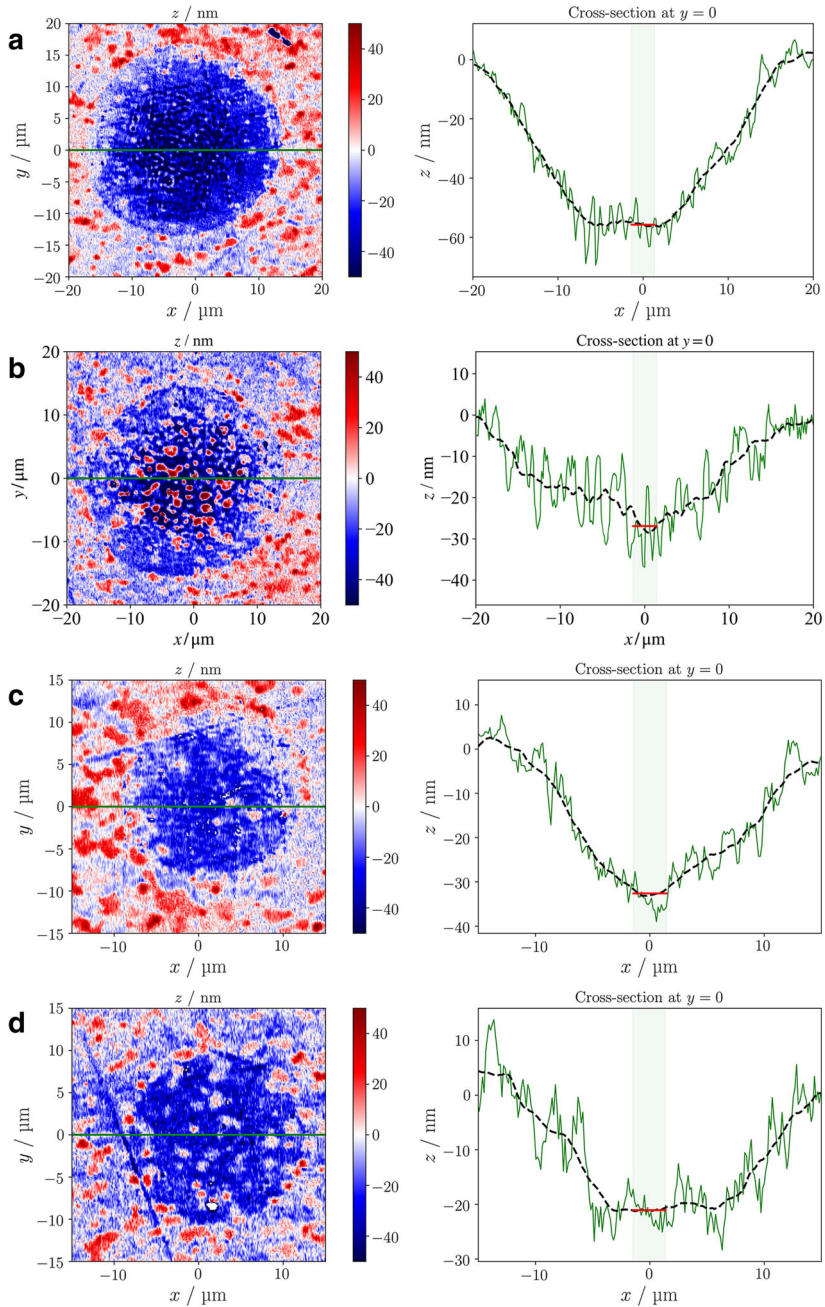
Fig. 7 Measured topology of the ablation structure using confocal microscopy for A: a fluence of 3.0 J/cm^2 and a pulse duration of 200 fs, B: 3.0 J/cm^2 and a pulse duration of 10 ps, C: 0.75 J/cm^2 and a pulse duration of 200 fs, D: 0.75 J/cm^2 and a pulse duration of 10 ps of the laser radiation. The green line in the left image represents the position of the cross-section on the right. The black dashed line in the right represents the moving average of the cross-section
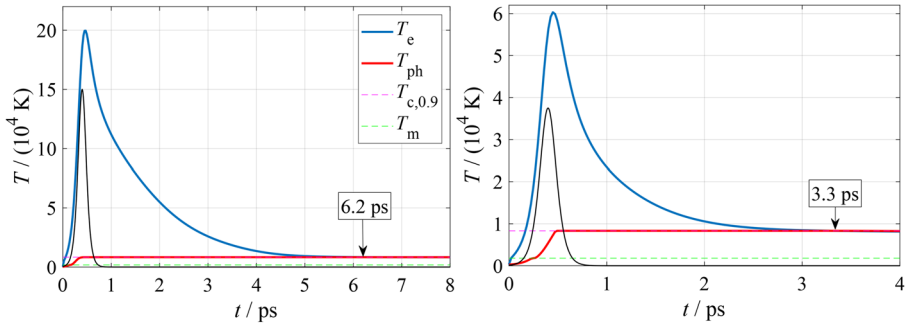
Fig. 8 Calculated temperature distribution at the irradiated material surface with a pulse duration of 200 fs and a fluence of left: $3.0 \, \text{J/cm}^2$ and right: $0.75 \, \text{J/cm}^2$. The blue line represents the electron temperature and the red line represents the phonon temperature. (The temporal distribution of the intensity is plotted schematically as a black line)

femtosecond regime and the reflectance is still comparatively high (Fig. 4). Furthermore, the time for diffusion and coupling between electrons and the phonon system is much longer for pulses in the picosecond regime than for pulses in the femtosecond regime. Consequently, at a constant fluence, the electron-phonon coupling time $\tau_{\text{e-ph}}$ is shorter for pulses in the femtosecond regime than in the picosecond regime. Using the pulse duration of 200 fs as an example, the coupling time at $0.75 \, \text{J/cm}^2$ equals 3.3 ps and at $3.0 \, \text{J/cm}^2$ 6.2 ps (Fig. 8). The phonon temperature can only increase up to $T_{\text{c},0.9}$ in the simulation, whereas the electron temperature also increases up to values much higher than $T_{\text{c},0.9}$. Additionally, the coupling factor is nearly independent on the electron temperature for high electron temperatures (Fig. 2), and more energy is absorbed by the material applying high fluences compared to a low fluence of the laser radiation. Thus, the coupling time increases for high fluences as the
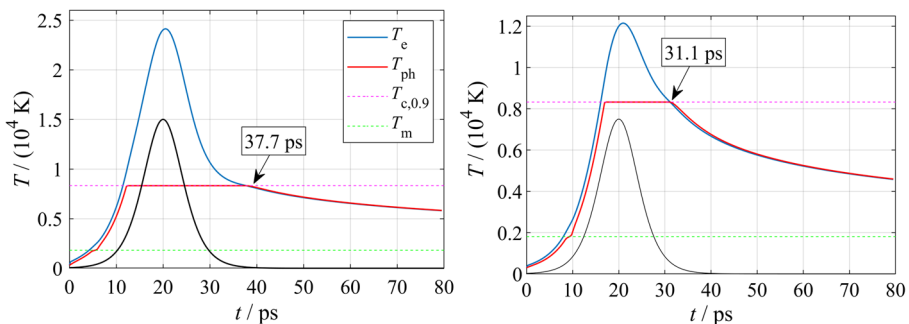

Fig. 9 Calculated temperature distribution at the irradiated material surface with a pulse duration of 10 ps and a fluence of left: $3.0 \, \text{J/cm}^2$ and right: $0.75 \, \text{J/cm}^2$. The blue line represents the electron temperature and the red line represents the phonon temperature. (The temporal distribution of the intensity is plotted schematically as a black line)

energy transfer from the electron to the phonon system and the phonon temperature are constant, whereas the electron temperature features much higher values.

The electron-phonon coupling time is also the time at which the coupling of the term $G(T_e - T_{ph})$ becomes zero and thus no further energy is transferred from the electron system to the phonon system. After the coupling time, the phonon temperature decreases below 90 % of the thermodynamic critical temperature $T_{c,\,0.9}$ due to heat conduction within the electron system into the material. In conclusion, no material will be ablated after the electron-phonon coupling time in this purely thermodynamic simulation.

Comparison Between the Simulated and the Calculated Ablation Depths

Based on the performed numerical calculations, the ablation depths are extracted from the simulations by determining the deepest position of $T_{c,0.9}$ along the z-axis for all time steps. The results are visualized in Fig. 10 and demonstrate, that at shorter pulse durations of the laser radiation, much deeper ablation depths are obtained. The calculated ablation depths in the low fluence regime are in good agreement with the experimentally determined values in this and other studies [5, 10, 13, 52, 63]. However, Fig. 10 illustrates that the experimentally determined ablation depths in the high fluence regime at 3.0 J/cm² are slightly lower than those of the simulations. The reflectance as a function of the electron temperature was approximated to the
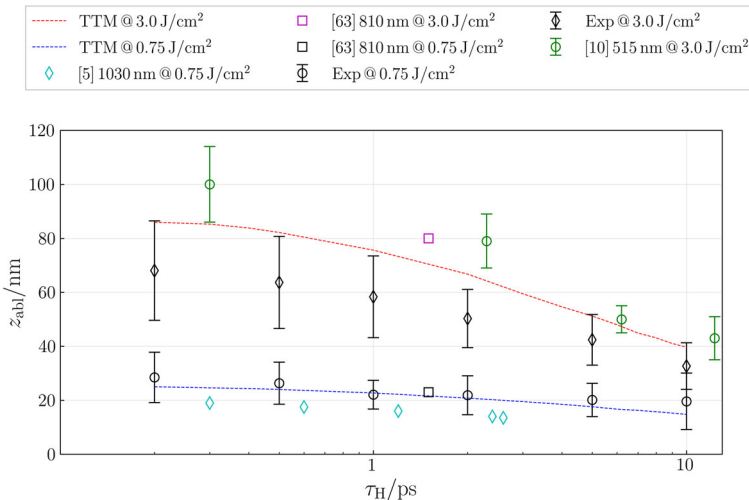

Fig. 10 Calculated ablation depth as a function of the pulse duration at a fluence of 0.75 J/cm² and 3.0 J/cm² compared to experimentally determined ablation depths. The black circles and diamonds are the experimentally determined ablation depths from this study

values of [25] with a regression function. Since the values of the DFT analysis were only performed up to an electron temperature of 25×10^3 K, the regression function can become slightly inaccurate at higher temperature, occurring in the high fluence regime. Furthermore, the reflectance might increase again with increasing electron temperature. Additionally, a strong shock wave is induced in the high fluence regime, which also might influence the ablation depths presented in [10] which were obtained with a wavelength of 515 nm and are slightly higher than those obtained from the performed simulations. Since the reflectance decreases more for smaller wavelengths than for larger wavelengths at high electron temperatures (Fig. 11), more energy is absorbed for $\lambda = 515$ nm than for $\lambda = 1030$ nm, and thus, a lower ablation threshold is obtained for $\lambda = 515$ nm. Another possible explanation for the relatively high difference at 3.0 J/cm^2 between the experimental and calculated ablation depths is that the shielding of the laser radiation by a possible early plasma formation is not considered.

Effective Penetration Depths

According to the calculated ablation depths from the simulations (Fig. 10), the effective penetration depths for both fluence regimes are calculated using Eqs. 15 and 16, respectively. Analogously to the ablation depth in Fig. 10, ablation of stainless steel using shorter pulse durations of the laser radiation results in a larger effective penetration depth. Furthermore, the effective penetration depth increases with increasing fluence as higher electron temperatures are observed resulting in an increased coupling time (e. g. the observed coupling times in Fig. 8 between 3.0 J/cm^2 and 0.75 J/cm^2) as well as in the increased thermal conductivity (Fig. 3). However, as can be seen in Fig. 12, the calculated values fit well to the determined experimental values from this study for 3 J/cm^2 in the high fluence regime, for 0.75 J/cm^2 in the low fluence regime, and are comparable to [10, 64].
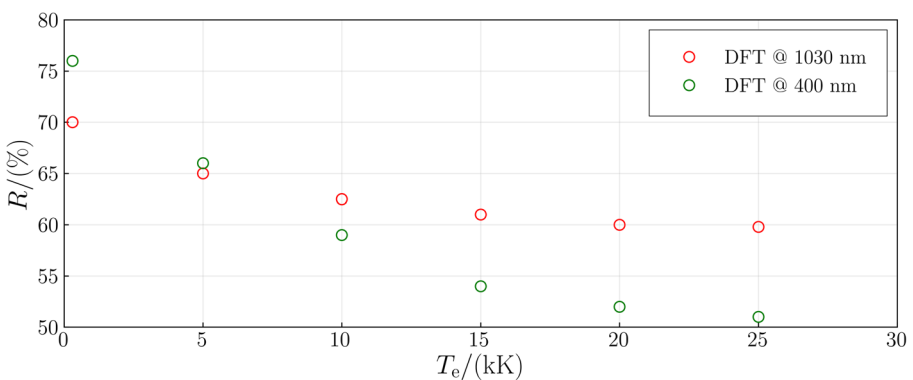

Fig. 11 Reflectance R as a function of the electron temperature T_e for iron at a wavelength $\lambda = 1030$ nm and $\lambda = 400$ nm based on [25]
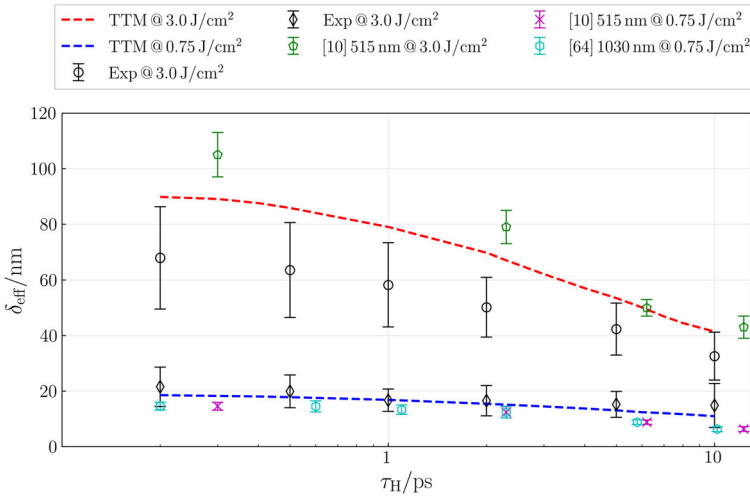
Fig. 12 Calculated effective penetration depth as a function of the pulse duration in comparison to experimental values from this study (black dots) and [10, 64]

Conclusions

The evolution of the temperature distribution of the electron- and phonon system of stainless steel heated by ultrafast laser radiation in the femtosecond up to the picosecond regime, has been calculated using the two temperature model. The simulations were performed for a bulk material with a linear absorption of the laser radiation, and temperature-dependent thermophysical parameters, like the coupling factor, the thermal conductivity and the volumetric heat capacity. Furthermore, no laser-induced compressive stresses were taken into account. The ablation criterium was defined as 90 % of the thermodynamic critical temperature of the phonon system, which can be assumed as the phase explosion. With this condition, the ablation depth was extracted from the simulations as a function of the fluence as well as of the pulse duration.

Ablation of stainless steel with pulse durations in the femtosecond regime results in larger ablation depths compared to pulse durations in the picosecond regime, in which the calculated ablation depths fit very well to the experimentally determined ones. Analogously to the calculated ablation depth, a significantly larger effective penetration depth was observed for pulse durations in the femtosecond regime, compared to the picosecond regime, which fits very well with the experimentally determined effective penetration depths.

Finally, a simplified model was presented, which considers no hydrodynamic processes and interaction of the ablated material with the laser radiation, but uses temperature dependent parameters. On the one hand, the simple model enables a calculation in a very short time and is therefore very relevant for industrial applications. On the other hand, the simple model describes the experimental values very well. Therefore, ablation results can be predicted very well without calculating more complex processes like hydrodynamics or thermal stress.

Compliance with Ethical Standards

Conflict of interests The authors declare that they have no conflict of interest.

References

1. Neuenschwander, B., Jaeggi, B., Schmid, M., Rouffiange, V., Martin, P.E.: In: Hennig, G., Xu, X., Gu, B., Nakata, Y. (eds.) Laser Applications in Microelectronic and Optoelectronic Manufacturing (LAMOM) XVII, vol. 8243, pp. 43–55 (2012). https://doi.org/10.1117/12.908583. International Society for Optics and Photonics, SPIE
2. Le Harzic, R., Huot, N., Audouard, E., Jonin, C., Laporte, P., Valette, S., Fraczkiewicz, A., Fortunier, R.: Comparison of heat-affected zones due to nanosecond and femtosecond laser pulses using transmission electronic microscopy. Appl. Phys. Lett. **80**(21), 3886 (2002)
3. Hirayama, Y., Obara, M.: Heat-affected zone and ablation rate of copper ablated with femtosecond laser. J. Appl. Phys. **97**(6), 064903 (2005)
4. Anisimov, S.I., Kapeliovich, B.L., Perelman, T.L.: Electron emission from metal surfaces exposed to ultrashort laser pulses. Zhurnal Eksperimentalnoi i. Teoreticheskoi Fiziki **66**, 776 (1974)
5. Artyukov, I., Zayarniy, D., Ionin, A.A., Kudryashov, S.I., Makarov, S.V., Saltuganov, P.N.: Relaxation phenomena in electronic and lattice subsystems on iron surface during its ablation by ultrashort laser pulses. JETP Lett. **99**(1), 51 (2014)
6. Gamaly, E.G., Madsen, N., Duering, M., Rode, A.V., Kolev, V.Z., Luther-Davies, B.: Ablation of metals with picosecond laser pulses: Evidence of long-lived nonequilibrium conditions at the surface. Phys. Rev. B **71**(17), 174405 (2005)
7. Bieda, M., Siebold, M., Lasagni, A.F.: Fabrication of sub-micron surface structures on copper, stainless steel and titanium using picosecond laser interference patterning. Appl. Surf. Sci. **387**, 175 (2016)
8. Nedialkov, N., Imamova, S., Atanasov, P., Heusel, G., Breitling, D., Ruf, A., Hügel, H., Dausinger, F., Berger, P.: Laser ablation of iron by ultrashort laser pulses. Thin Solid Films **453**, 496 (2004)
9. Nedialkov, N., Atanasov, P., Imamova, S., Ruf, A., Berger, P., Dausinger, F.: Dynamics of the ejected material in ultra-short laser ablation of metals. Appl. Phys. A **79**(4-6), 1121 (2004)
10. Smirnov, N.A., Kudryashov, S.I., Danilov, P.A., Rudenko, A.A., Gakovic, B., Milovanović, D., Ionin, A.A., Nastulyavichus, A.A., Umanskaya, S.F.: Microprocessing of a steel surface by single pulses of variable width. Laser. Phys. Lett. **16**(5), 056002 (2019). https://doi.org/10.1088/1612-202X/ab0c85. https://iopscience.iop.org/article/10.1088/1612-202X/ab0c85/pdf
11. Momma, C., Nolte, S., Chichkov, B.N., Alvensleben, F.V., Tünnermann, A.: Precise laser ablation with ultrashort pulses. Appl. Surface. Sci. **109**, 15 (1997)
12. Nolte, S., Momma, C., Jacobs, H., Tünnermann, A., Chichkov, B.N., Wellegehausen, B., Welling, H.: Ablation of metals by ultrashort laser pulses. JOSA B **14**(10), 2716 (1997)

13. Le Harzic, R., Breitling, D., Weikert, M., Sommer, S., Föhl, C., Valette, S., Donnet, C., Audouard, E., Dausinger, F.: Appl. Surf. Sci. **249**(1-4), 322 (2005). https://doi.org/10.1016/j.apsusc.2004.12.027

14. Jaeggi, B., Neuenschwander, B., Schmid, M., Muralt, M., Zuercher, J., Hunziker, U.: Influence of the pulse duration in the ps-regime on the ablation efficiency of metals. Phys. Procedia. **12**, 164 (2011)

15. Jee, Y., Becker, M.F., Walser, R.M.: Laser-induced damage on single-crystal metal surfaces. JOSA B **5**(3), 648 (1988)

16. Di Niso, F., Gaudiuso, C., Sibillano, T., Mezzapesa, F.P., Ancona, A., Lugarà, P.M.: Role of heat accumulation on the incubation effect in multi-shot laser ablation of stainless steel at high repetition rates. Optics Express **22**(10), 12200 (2014)

17. Byskov-Nielsen, J., Savolainen, J.M., Christensen, M.S., Balling, P.: Appl. Phys. A **101**(1), 97 (2010). https://doi.org/10.1007/s00339-010-5766-1

18. Kononenko, T., Garnov, S., Klimentov, S., Konov, V., Loubnin, E., Dausinger, F., Raiber, A., Taut, C.: Appl. Surf. Sci. **48**, 109–110 (1997). https://doi.org/10.1016/S0169-4332(96)00905-1

19. Kanavin, A.P., Afanasiev, Y.V., Chichkov, B.N., Isakov, V.A., Smetanin, I.V.: SPIE Proceedings. SPIE, p. 446. https://doi.org/10.1117/12.376993 (1999)

20. Abdelmalek, A., Bedrane, Z., Amara, E.H.: J. Phys. Conference Series **987**(1), 012012 (2017). https://doi.org/10.1088/1742-6596/987/1/012012. https://iopscience.iop.org/article/10.1088/1742-6596/987/1/012012/pdf

21. Jia, X., Zhao, X.: Numerical study of material decomposition in ultrafast laser interaction with metals. Appl. Surf. Sci. **463**, 781 (2019)

22. Sotrop, J., Domke, M., Kersch, A., Huber, H.P.: Phys. Procedia. **41**, 520 (2013). https://doi.org/10.1016/j.phpro.2013.03.110

23. Bévillon, E., Colombier, J.P., Dutta, B., Stoian, R.: J. Phys. Chem. C **119**(21), 11438 (2015). https://doi.org/10.1021/acs.jpcc.5b02085

24. Graves, R.S., Kollie, T.G., McElroy, D.L., Gilchrist, K.E.: Int. J. Thermophys. **12**(2), 409 (1991). https://doi.org/10.1007/BF00500761

25. Bévillon, E., Stoian, R., Colombier, J.P.: J. Phys. Condensed Matter:an. Institute of Physics Journal **30**(38), 385401 (2018).

26. Sun, C.K., Vallée, F., Acioli, L.H., Ippen, E.P., Fujimoto, J.G.: Phys. Rev. B **50**, 15337 (1994). https://doi.org/10.1103/PhysRevB.50.15337

27. Olbrich, M., Punzel, E., Lickschat, P., Weißmantel, S., Horn, A.: Phys. Procedia. **83**, 93 (2016). https://doi.org/10.1016/j.phpro.2016.08.017. Laser Assisted Net Shape Engineering 9 International Conference on Photonic Technologies Proceedings of the LANE 2016 September 19–22, 2016 Fürth, Germany

28. Paltauf, G., Dyer, P.E.: Chem. Rev. **103**(2), 487 (2003). https://doi.org/10.1002/chin.200318290

29. Zhigilei, L.V., Lin, Z., Ivanov, D.S.: J. Phys. Chem. C **113**(27), 11892 (2009). https://doi.org/10.1021/jp902294m

30. Olbrich, M., Pflug, T., Wüstefeld, C., Motylenko, M., Sandfeld, S., Rafaja, D., Horn, A.: Optics and Lasers in Engineering **129**, 106067 (2020). https://doi.org/10.1016/j.optlaseng.2020.106067. http://www.sciencedirect.com/science/article/pii/S0143816619311030

31. Fucke, W., Seydel, U.: Improved experimental determination of critical-point data for tungsten. High Temperatures-High Pressures **12**(4), 419 (1980)

32. Xu, X.: Phase explosion and its time lag in nanosecond laser ablation. Appl. Surf. Sci. **197**, 61 (2002)

33. Khishchenko, K.: J. Phys.: Conf. Ser, 121. https://doi.org/10.1088/1742-6596/121/2/022025 (2008)

34. Lomonosov, I.: AIP Conference Proceedings, vol. 955. (American Institute of Physics) **955**, 63–66 (2007). https://doi.org/10.1017/S0263034607000687

35. Fortov, V., Lomonosov, I.: The Open Plasma Physics Journal 3(1). https://doi.org/10.2174/1876534301003010122 (2010)

36. Povarnitsyn, M.E., Fokin, V.B., Levashov, P.R.: Appl. Surf. Sci. **357**, 1150 (2015). https://doi.org/10.1016/j.apsusc.2015.09.131

37. Povarnitsyn, M.E., Itina, T.E., Sentis, M., Khishchenko, K., Levashov, P.: Phys. Rev. B **75**(23), 235414 (2007). https://doi.org/10.1103/PhysRevB.75.235414

38. Povarnitsyn, M.E., Itina, T.E., Levashov, P.R., Khishchenko, K.V.: Appl. Surface Sci. **257**(12), 5168 (2011). https://doi.org/10.1016/j.apsusc.2010.11.158

39. Povarnitsyn, M.E., Itina, T.E., Levashov, P.R., Khishchenko, K.V.: Phys. Chem. Chem. Phys. **15**(9), 3108 (2013). https://doi.org/10.1039/C2CP42650A

40. Bashir, S., Rafique, M.S., Husinsky, W.: Radiation Effects and Defects in Solids **168**(11–12), 902 (2013). https://doi.org/10.1080/10420150.2013.784911
41. Villerius, V., Kooiker, H., Post, J., Pei, Y.T.: Int. J. Mach. Tools. Manuf. **138**, 27 (2019). https://doi.org/10.1016/j.ijmachtools.2018.11.003
42. Bulgakova, N.M., Bourakov, I.M.: Appl. Surf. Sci. **41**, 197–198 (2002). https://doi.org/10.1016/S0169-4332(02)00300-8
43. Chen, J.K., Beraun, J.E.: J. Opt. A. Pure. Appl. Opt. **5**(3), 168 (2003). https://doi.org/10.1088/1464-4258/5/3/304
44. Kelly, R., Miotello, A.: Appl. Surf. Sci. **205**, 96–98 (1996). https://doi.org/10.1016/0169-4332(95)00481-5
45. Colombier, J.P., Combis, P., Bonneau, F., Le Harzic, R., Audouard, E.: Phys. Rev. B **71**(16), 165406 (2005)
46. Förster, D.J., Faas, S., Gröninger, S., Bauer, F., Michalowski, A., Weber, R., Graf, T.: Shielding effects and re-deposition of material during processing of metals with bursts of ultra-short laser pulses. Appl. Surf. Sci. **440**, 926 (2018)
47. Wellershoff, S.S., Hohlfeld, J., Güdde, J., Matthias, E.: Appl. Phys. A. Mater. Sci. Process. **69**(S1), S99 (1999). https://doi.org/10.1007/s003399900305
48. Valencia, J.J., Quested, P.N.: Thermophysical properties (2013)
49. Gray, D.E.: American Institute of Physics (AIP). Handbook. AIP Advances (1972)
50. Sipkens, T.A., Hadwin, P.J., Grauer, S.J., Daun, K.J.: Predicting the heat of vaporization of iron at high temperatures using time-resolved laser-induced incandescence and Bayesian model selection. J. Appl. Phys. **123**(9), 095103 (2018)
51. Schönecker, S., Li, X., Johansson, B., Kwon, S.K., Vitos, L.: Thermal surface free energy and stress of iron. Sci. Rep. **5**, 14860 (2015)
52. Mannion, P., Magee, J., Coyne, E., O'Connor, G., Glynn, T.: Appl. Surf. Sci. **233**(1-4), 275 (2004). https://doi.org/10.1016/j.apsusc.2004.03.229
53. Chen, F., Du, G., Yang, Q., Si, J., Hou, H.: In: Ahsan, A. (ed.) Two phase flow, phase change and numerical modeling. InTech, Rijeka (2011). https://doi.org/10.5772/21031
54. Gan, Y., Qi, W., Shen, Y., Chen, Z.: Optics. Lett. **38**(14), 2397 (2013). https://doi.org/10.1364/OL.38.002397
55. Huang, J., Zhang, Y., Chen, J.K.: Numerical Heat Transfer, Part A: Applications **57**(12), 893 (2010). https://doi.org/10.1080/10407782.2010.489491
56. Rethfeld, B., Ivanov, D.S., Garcia, M.E., Anisimov, S.I.: J. Phys. D:. Appl. Phys. **50**(19), 193001 (2017). https://doi.org/10.1088/1361-6463/50/19/193001
57. Chichkov, B.N., Momma, C., Nolte, S., Alvensleben, F., TÜNnermann, A.: Appl. Phys. A Mater. Sci. Process. **63**(2), 109 (1996). https://doi.org/10.1007/BF01567637
58. Hashida, M., Semerok, A., Gobert, O., Petite, G., Izawa, Y., Wagner, J.: Appl. Surface Sci. **862**, 197–198 (2002). https://doi.org/10.1016/S0169-4332(02)00463-4
59. Preuss, S., Demchuk, A., Stuke, M.: Appl. Phys. A. Mater. Sci. Process. **61**(1), 33 (1995). https://doi.org/10.1007/BF01538207
60. Mannion, P., Magee, J., Coyne, E., O'Connor, G.M.: SPIE Proceedings. SPIE, p 470. https://doi.org/10.1117/12.463744 (2002)
61. Christensen, B.H., Vestentoft, K., Balling, P.: Short-pulse ablation rates and the two-temperature model. Appl. Surf. Sci. **253**(15), 6347 (2007)
62. Danilov, P., Ionin, A., Khmelnitskii, R., Kiseleva, I., Kudryashov, S., Mel'nik, N., Rudenko, A., Smirnov, N., Zayarny, D.: Appl. Surf. Sci. **425**, 170 (2017). https://doi.org/10.1016/j.apsusc.2017.06.289
63. Wynne, A.E., Stuart, B.C.: Appl. Phys. A **76**(3), 373 (2003). https://doi.org/10.1007/s00339-002-1823-8
64. Lickschat, P., Metzner, D., Weissmantel, S.: Journal of Advanced Manufacturing Technology. https://doi.org/10.1007/s00170-020-05502-8 (2020)